# Supplementary Materials for

## Unidirectionally excited phonon polaritons in high-symmetry orthorhombic crystals

Qing Zhang *et al.*

Corresponding author: Qingdong Ou, qingdong.ou@monash.edu; Andrea Alù, aalu@gc.cuny.edu;
Rainer Hillenbrand, r.hillenbrand@nanogune.eu; Cheng-Wei Qiu, chengwei.qiu@nus.edu.sg

**This PDF file includes:**

Sections S1 to S8
Figs. S1 to S14
References

## 1. Dielectric functions of biaxial orthorhombic crystal α-MoO₃

The optical response of the α-MoO₃ is dominated by the phonon absorption, thus its dielectric tensor can be calculated by using a Lorentz model (*40, 23*):

$$\varepsilon_j(\omega) = \varepsilon_\infty^j \left(1 + \frac{\omega_{LO}^{j\,2} - \omega_{TO}^{j\,2}}{\omega_{TO}^{j\,2} - \omega^2 - i\omega\gamma^j}\right) , \quad j = x, y, z, \tag{S1}$$

VdW material α-MoO₃ is an anisotropic material ($\hat{\varepsilon} = \text{diag}\{\varepsilon_x, \varepsilon_y, \varepsilon_z\}$, $\varepsilon_x \neq \varepsilon_y \neq \varepsilon_z$), where $x$, $y$, and $z$ denote the three principal axes of the crystal, which correspond to the crystalline directions [100], [001], and [010], respectively. $\omega_{TO}$ and $\omega_{LO}$ refer to the *TO* and *LO* phonon frequencies. Parameter $\varepsilon_\infty$ is the high frequency dielectric constant, and $\gamma$ is the broadening factor of the Lorentzian line shape. The fitting parameters are listed in Table S1.
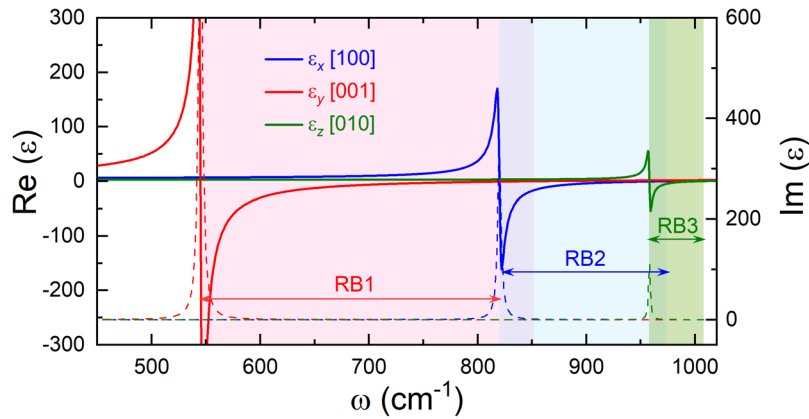


**Fig. S1 | The permittivities of α-MoO₃**. The real part (solid lines) and image part (dashed lines) permittivities of α-MoO₃ at three crystalline directions. Reststrahlen bands are shaded in different colors.

| Direction | x [100] | y [001] | z [010] |
|---|---|---|---|
| $\varepsilon_\infty$ | 4 | 5.2 | 2.4 |
| $\omega_{TO}$ / cm⁻¹ | 820 | 545 | 958 |
| $\omega_{LO}$ / cm⁻¹ | 972 | 851 | 1004 |
| $\gamma$ / cm⁻¹ | 4 | 4 | 2 |

**Tab. S1 | Parameters used for calculating the permittivities of α-MoO₃ (equation S1).**

## 2. Analytical dispersion of the biaxial α-MoO₃

The dispersion (or isofrequency surface) of biaxial crystal α-MoO₃ can be obtained from the well-known Fresnel's equation for biaxial media. In the coordinate system, the $x$, $y$ and $z$-axis correspond to the crystalline directions [100], [001], and [010] of the α-MoO₃, respectively. The dielectric permittivity tensor $\hat{\varepsilon}$ of α-MoO₃ can be expressed as,

$$\hat{\varepsilon} = \begin{pmatrix} \varepsilon_x & 0 & 0 \\ 0 & \varepsilon_y & 0 \\ 0 & 0 & \varepsilon_z \end{pmatrix} \tag{S2}$$

We start from the Maxwell equation,

$$\nabla \cdot \vec{D} = 0$$
$$\nabla \cdot \vec{B} = 0$$
$$\nabla \times \vec{E} = i\omega\vec{B} \tag{S3}$$
$$\nabla \times \vec{H} = -i\omega\vec{D}$$
$$\vec{D} = \varepsilon_0 \hat{\varepsilon} \vec{E}, \ \vec{B} = \mu_0 \vec{H}$$

By substituting the plane wave solution into the Maxwell equation we can obtain the following relations

$$\vec{k} \cdot \vec{D} = 0$$
$$\vec{k} \cdot \vec{B} = 0$$
$$\vec{k} \times \vec{E} = \omega\vec{B} \tag{S4}$$
$$\vec{k} \times \vec{H} = -\omega\vec{D}$$

By solving above equations and substituting the magnetic field $H$, we then obtain that

$$\vec{k} \times (\vec{k} \times \vec{E}) + k_0^2 \hat{\varepsilon}\vec{E} = 0$$
$$\vec{k}(\vec{k} \cdot \vec{E}) - k^2\vec{E} + k_0^2\hat{\varepsilon}\vec{E} = 0 \tag{S5}$$

Finally, we can substitute Eq. (S2) into Eq. (S5), and write the equations as a matrix form

$$\begin{pmatrix} k_0^2\varepsilon_x - (k_y^2 + k_z^2) & k_x k_y & k_x k_z \\ k_x k_y & k_0^2\varepsilon_x - (k_y^2 + k_z^2) & k_y k_z \\ k_x k_z & k_y k_z & k_0^2\varepsilon_x - (k_y^2 + k_z^2) \end{pmatrix}\begin{pmatrix} E_x \\ E_y \\ E_z \end{pmatrix} = M\vec{E} = 0 \tag{S6}$$

The Eq. (S6) has nontrivial solutions only when det($M$) = 0, that gives the dispersion for biaxial crystal α-MoO₃,

$$(\varepsilon_x k_x^2 + \varepsilon_y k_y^2 + \varepsilon_z k_z^2)(k_x^2 + k_y^2 + k_z^2) + \varepsilon_x\varepsilon_y\varepsilon_z k_0^4$$
$$-k_0^2[\varepsilon_x(\varepsilon_y + \varepsilon_z)k_x^2 + \varepsilon_y(\varepsilon_x + \varepsilon_z)k_y^2 + \varepsilon_x(\varepsilon_x + \varepsilon_y)k_z^2] = 0 \tag{S7}$$

For instance, Fig. S2a shows the 3D isofrequency surface at RB-II frequency 930 cm$^{-1}$, the opening direction of unbounded hyperbolic isofrequency surface is along the [100] axis where the permittivity is negative. As for the in-plane dispersion of volume-confined PhPs in α-MoO₃ slab, it can be analytically calculated by recently derived formalism (41, 42),

$$q = \frac{\rho}{k_0 d} \left[ \arctan\left(\frac{\varepsilon_1 \rho}{\varepsilon_z}\right) + \arctan\left(\frac{\varepsilon_3 \rho}{\varepsilon_z}\right) + \pi l \right], l = 0,1,2....$$ (S8)

where $\rho = i\sqrt{\varepsilon_z q^2 / (\varepsilon_x q_x^2 + \varepsilon_y q_y^2)}$, $m$ is the order of TM modes, $q = \sqrt{(k_x/k_0)^2 + (k_y/k_0)^2}$ is the normalized in-plane momentum, $d$ is the thickness of the α-MoO₃ slab, $\varepsilon_1$ and $\varepsilon_3$ are the permittivities of the superstrate and substrate, respectively. The white dashed line in Fig. S2b is the analytical result.
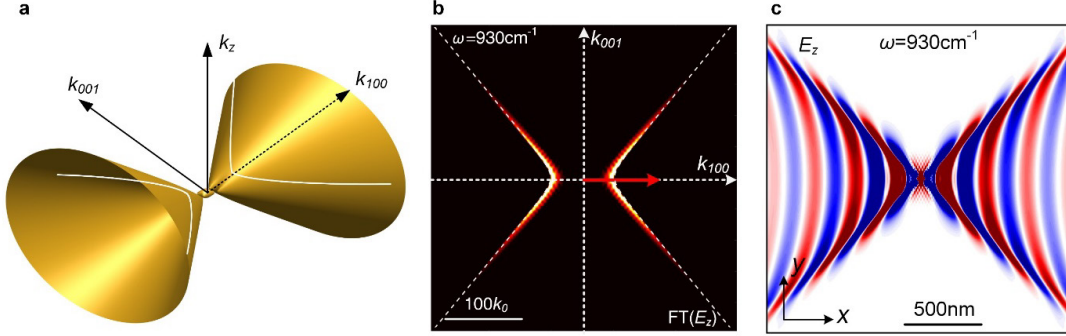


**Fig. S2 | The dispersion and propagating behavior of PhPs in biaxial α-MoO₃.** (a) 3D iso-frequency surface observed in Reststrahlen Band-II ($\varepsilon_x < 0 < \varepsilon_y < \varepsilon_z$). (b) The in-plane isofrequency contour of the 50 nm-thick α-MoO₃ slab at frequency $\omega$=930 cm$^{-1}$. The back-ground isofrequency contour is the Fourier Transforms of $E_z$ [FT($E_z$)]. The white dashed line is the analytical result according to Eq. S8. (c) The $E_z$ field distribution of PhPs excited by a $z$-polarized dipole.

## 3. Symmetric diffraction of PhPs in h-BN

We first discuss the grating diffraction of PhPs in in-plane isotropic vdW material h-BN. Similar as the conventional diffraction in free-space, the in-plane diffraction of PhPs in h-BN requires the grating period larger than the polariton wavelength ($\Lambda > \lambda_p$). Due to the in-plane circular isofrequency contour [yellow dashed circles in Fig. S3(g-i)], the diffraction only depends on the grating period and the polariton wavelength according to $\Lambda\cos\theta = m\lambda_p$. As shown in Fig. S3(a, d), when incident polarization $E$ is perpendicular to the gating, the zero-order diffraction is much stronger than the ±1$^{st}$ order diffraction, showing wavefront propagating parallel to the grating. When the incident polarization is parallel to the grating (Fig. S3b), four diffraction states are excited with circular-hole grating, showing cross-shaped diffraction pattern (Fig. S3e). The corresponding FT spots in Fig. S3h are exactly located at the intersections between the vertical line along $k_G$ and the circular isofrequency curve. As for blaze grating design (Fig. S3c), only the forward +1$^{st}$ diffraction order is excited, illustrating a forward shockwave along the grating (Fig. S3f). In addition, as shown in Fig. S3i, we also observed two bright spots at $k_x$=0. These two spots are the zero-order diffraction states that are perpendicular to the grating. In contrast, the zero-order grating diffraction is forbidden in α-MoO₃ with no intersection at $k_x$=0 with the hyperbolic isofrequency curve. This forbidden zero-order diffraction allows better observation of the directional 1$^{st}$ order PhPs as discussed below. Moreover, we can see that two bright spots in the FT at positive $k_x$ because the maximum diffraction efficiency is blazed to the forward +1$^{st}$ diffraction order.
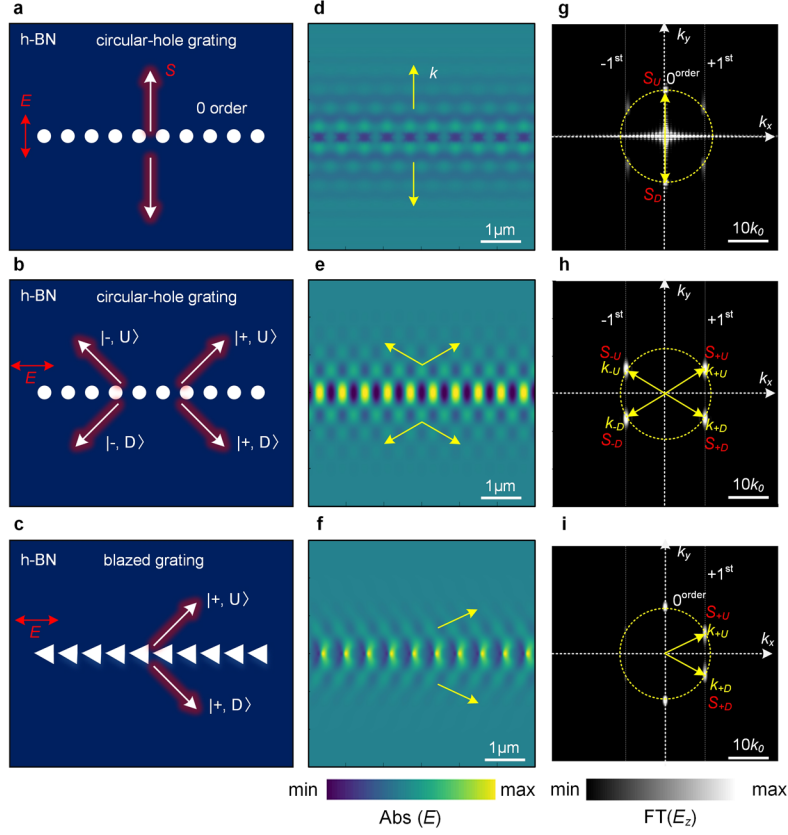
**Fig. S3 | In-plane diffraction of PhPs in h-BN.** (a-c) Schematic of PhPs diffraction in h-BN by circular-nanohole and blazed gratings. The grating period $\Lambda$=600 nm, circular-nanohole diameter 300 nm, triangle size 600×400 nm, and the h-BN thickness $d$=200 nm. Red arrows indicate the energy flow $S$ (or wavevector $k$) for each diffraction state. (d-f) Numerically simulated electric field distribution Abs ($E$) of the PhPs excited by gratings in (a-c) at frequency $\omega$=1580 cm$^{-1}$. The yellow arrows indicate the wavevector of each diffraction state. (g-i) Fourier transforms of the simulated field distributions $E_z$ shown in (d-f). The yellow dashed circles show the analytical isofrequency contours of PhPs in h-BN.

## 4. Rotation angle dependent asymmetric diffraction of PhPs in α-MoO₃

To fully address the directional control of grating-PhPs in α-MoO₃, we exploit a rotation-controlled isofrequency surface $f(k_x, k_y, \varphi) = 0$ to trace the implicit relations between diffraction angle, grating constant and rotation angle. A rotation matrix $R(\varphi)$ is used to transform the dispersion in Eq. S8 from α-MoO₃'s principal axes coordinate ($k_{100}$, $k_{001}$) to Cartesian coordinate ($k_x$, $k_y$),

$$\begin{bmatrix} k_{100} \\ k_{001} \end{bmatrix} = \begin{bmatrix} \cos\varphi & \sin\varphi \\ -\sin\varphi & \cos\varphi \end{bmatrix} \begin{bmatrix} k_x \\ k_y \end{bmatrix} = R(\varphi) \begin{bmatrix} k_x \\ k_y \end{bmatrix} \tag{S9}$$

Substituting Eq. S9 into Eq. S8, we obtain the rotation-related isofrequency surface (Fig. S3). Supposing that the grating period $\Lambda$=600 nm, we obtain the grating's reciprocal lattice vector $k_G$=±2π/$\Lambda$. Through vertical cutting of the isofrequency surface at $k_x$=$k_G$, the $k_y$ components of four diffraction states $|\pm, L \text{ or } R\rangle$ versus $\varphi$ can be achieved. As a result, the corresponding diffraction angles are equal to $\theta$= arctan($k_y$/$k_G$). Note that for calculating experimental diffraction angles of

tip-launched PhPs (Fig. 3c), the isofrequency curves should be multiplied by a factor of two in Eq.S9, because the experimentally obtained fringe spacing is $\lambda_p/2$ owing to doubled optical path, as we discussed below.
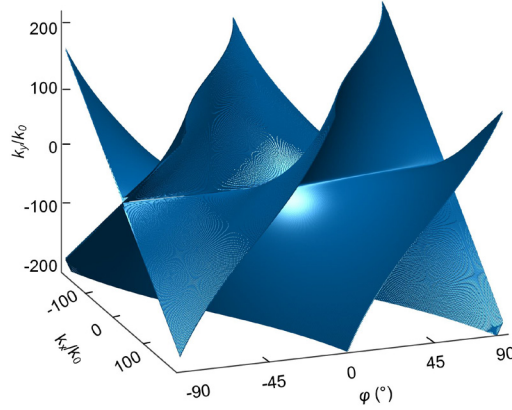


**Fig. S4 | The rotation-controlled isofrequency surface.** 3D isofrequency surface as a function of rotation angle φ (that is the relation between $k_x$, $k_y$ and rotation angle $\varphi$) for 220 nm-thick α-MoO₃ slab at frequency 904 cm$^{-1}$.

## 5. Unidirectional diffraction of PhPs in α-MoO₃

With blazed grating design (Fig. S5a), one can steer the maximized diffraction efficiency into the +1$^{st}$ order, so only forward PhPs can be generated. In free-space, it's well known that the interference pattern from the grating is just the production of the diffraction from a single-slit (single triangle hole) and the interference from multiple-slits (a series triangle-hole array). We assume that the blazing angle α=<**a, c**>, and the PhPs are excited at the **c** edge. Note that for hyperbolic PhPs, the direction of the energy flow ($S$, red arrays in Fig. S5a) is perpendicular to the tangent of the hyperbolic isofrequency contour. For causality reasons, $S$ always points away from the grating, even though the wavefronts (determined by $k$, blue arrows in Fig. S5a) propagate towards the grating, corresponding to backward propagation. Thus, the corresponding optical path difference between two grating elements is $\Delta L=\Lambda \sin\alpha=m\lambda_\varphi$, where m is the diffraction order, and $\lambda_\varphi$ is the wavelength of grating excited PhP at grating orientation angle $\varphi$. Accordingly, the +1$^{st}$ order diffraction of PhPs by such a polaritonic blazing grating should satisfy the condition of $\sin\alpha=k_G/k_\varphi$. Fig. S5b shows the grating efficiency of each diffraction order. The blue (red) line denotes the intensity of multiple slits interference (single-slit diffraction) component, and the red contour denotes maximum grating efficiency is concentrated in the +1$^{st}$ order.

**Case-1 (blazing +1$^{st}$ order diffraction of PhPs at $\varphi=0°$):** In the case of blazed grating with orientation angle $\varphi=0°$, the calculated blazed angle $\alpha=48°$, and the corresponding diffraction states are marked by two black circles in Fig. R3c. With this grating design [Fig. S5(d1)], we observed strong and smooth wavefront at both two-sides of the grating in Fig. S5(d2), in comparison to other results in Fig. S5.

**Case-2 (blazing +1$^{st}$ order diffraction of unidirectional PhPs at $\varphi=25°$):** In the case of blazed grating with orientation angle $\varphi=25°$, the iso-frequency contour (red line in Fig. S5c) only has one crossing point (red circle) at $k_G$, which hence yields the unidirectional diffraction of PhPs [Fig. S5(e3)]. The calculated blazed angle $\alpha=82°$ (in experiments $\alpha$ is set as 90°).

**Case-3 (blazing +1$^{st}$ order diffraction of PhPs at $\varphi$=60°):** In the case of blazed grating with orientation angle $\varphi$=60°, the effect of blazed grating is not as effective as the previous two designs [Fig. S5(f4)]. The first reason is the zero order diffraction at $k_G$=0, and the second reason is that the **b** edge also excites -1$^{st}$ order diffracted PhPs.
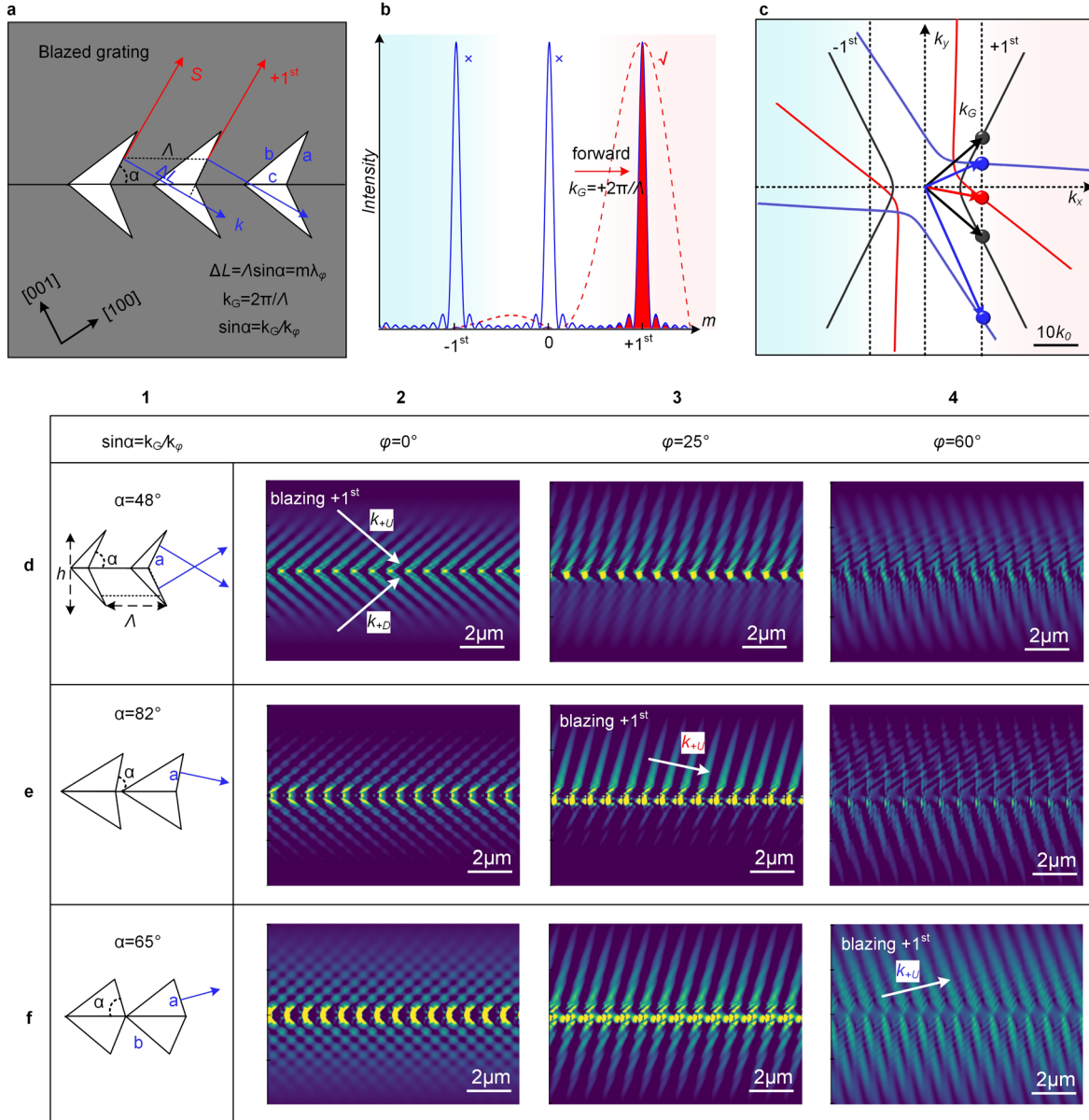


**Fig. S5 | Diffraction of PhPs by blazing grating in α-MoO₃.** (a) The schematic of the blazed grating, the thickness of the flake is 182 nm, with grating period $\Lambda$=800 nm, $h$=1000 nm. (b) The diffraction efficiency of each diffraction order. The blue (red) dashed line denotes the interference (diffraction) component of the grating, and the red contour denotes the total efficiency of the +1$^{st}$ order. (c) Isofrequency contours of the PhPs for different grating orientations relative to the [100] crystal direction of α-MoO₃ ($\varphi$=0°, 25° and 60°, respectively) at frequency 904 cm$^{-1}$. The symbols denote the diffraction wavevectors of diffracted PhPs at each rotation angle. (d-f) Numerically simulated abs($E_x$) field distributions with various triangular gratings and different orientation angles.

## 6. Simulations and experiments of grating and tip launched PhPs

The FDTD simulations (Lumerical FDTD Solutions) were employed to calculate the wavefronts of diffracted PhPs. The nano-hole grating array is placed inside the α-MoO$_3$ slab. Perfected matched layer (PML) absorbing boundary conditions are set at all simulation boundaries in Fig. S6d. A permittivity rotation analysis group is modeled on the α-MoO$_3$ slab, which can be used to control the orientation angle ($\varphi$) between grating direction and α-MoO$_3$'s [100] crystal direction. Hence, we can numerically calculate the electric field distribution of grating-PhPs at each RB frequency with different rotational angle. To excite PhPs, we use a plane wave source to normally illuminate the grating with polarization parallel to the grating. Each nano-hole working as a dipole source generates hyperbolic wavefront with spacing $\lambda$ (Fig. S6a), so their collective interference leads to plane-wave-like wavefront with fringe spacing $\lambda_s$ (Fig. S6d). As shown in Fig. S6e, it's clear that the momentum matching occurs at the $k_p$ isofrequency curve (white dashed line). While in experiments (Fig. S6b, c), the PhPs are efficiently launched by AFM tip, which are reflected back to the tip at nano-hole's boundaries and interfere at the tip apex with the local field. Recording the tip-scattered field yields interference fringes with spacing $\lambda/2$. Thus, the experimental momentum matching occurs at $2k_p$ isofrequency curve (green dashed line) (Fig. S6g). The difference also lies in the diffraction angles between simulations and experiments. At the vertical red dashed line of $k_G=2\pi/\Lambda$, the simulated wavevector $k_s$ is larger than that of the experimental wavevector $k_e$, leading to different $\theta_s$ and $\theta_e$. More comparisons between simulations and experiments are shown in Fig. S8.
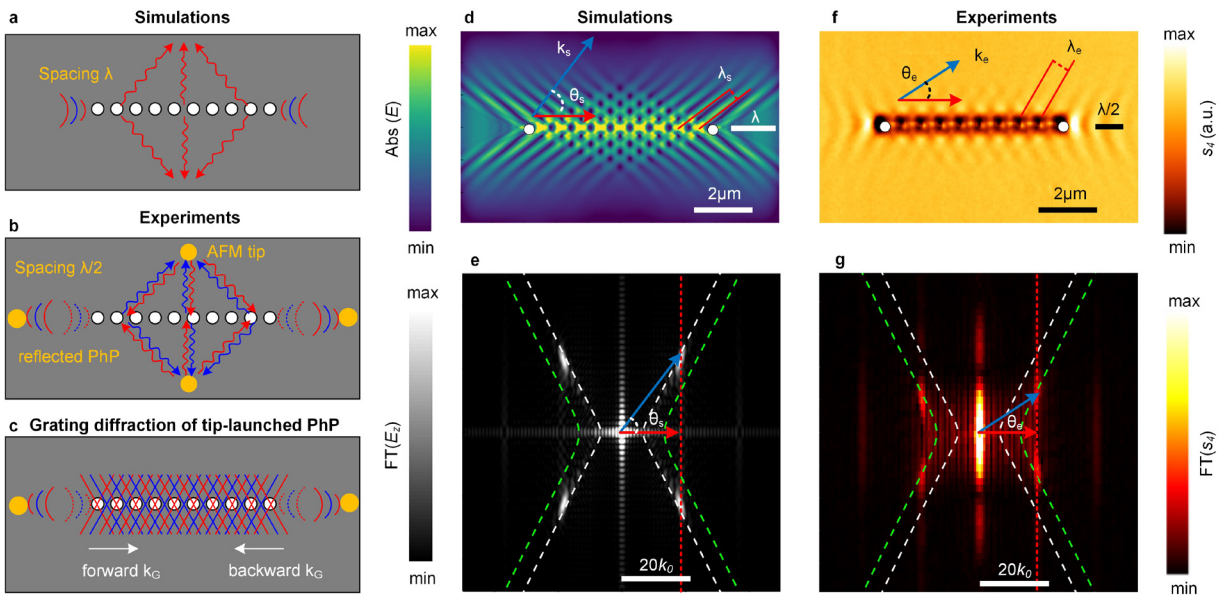


**Fig. S6 | Simulations and experiments of grating and tip launched PhPs.** Schematics of (a) numerical simulation of grating excited PhPs and (b, c) experimental observations of tip-launched PhPs. (d) The simulated electric field distribution *abs(E)* of PhPs excited by circular nano-hole grating ($\Lambda$=600 nm, and diameter 300 nm) in 220 nm-thick α-MoO$_3$ sample at rotation angle $\varphi$=0°, the frequency $\omega$=904 cm$^{-1}$. (e) The bright spots are the FT($E_z$) of simulated PhPs in (d). The white dashed line is analytical result calculated according to Eq. (S8), while green dashed line belongs to $2k_{100}$. (f, g) The experimentally measured near-field signals ($s_4$) and FT($s_4$) of the diffracted tip-launched PhPs.

## 7. Phenomenological interference model

The experimentally measured near-field distributions of the tip-launched PhPs can be calculated using a phenomenological interference model, as schematically shown in Fig. S7. The circular-hole grating (Fig. S7a) could be considered as $m$ nano-hole cavities. Each nano-cavity has $n$ boundary edges, in which the tip-launched PhPs are reflected back to the tip and interfere with the tip-launched wave. So the total field distributions are the interference pattern with all nano-hole launched waves, and can be described as:

$$\psi = \tilde{\psi}_{PhPs,0} + \sum_m \sum_n \tilde{\psi}_{PhPs,(n,m)} \tag{S10}$$

where $\tilde{\psi}_{PhPs,0}$ is the tip-launched PhPs. The reflected waves from nano-hole $m$ and edge $n$ can be described as (27, 28):

$$\tilde{\psi}_{PhPs,(n,m)} = R_{(n,m)} \times \tilde{\psi}_{PhPs,0} \exp\left[-2\,\mathrm{Re}(q) r_{(n,m)}(\gamma + i)\right] \tag{S11}$$

where $R_{(n,m)} = R_0 \exp(i\Delta\varphi)$ denotes the complex reflection coefficient, which includes the reflectivity $R_0$ and phase shift of the polariton wave, $\gamma$ and $r_{(n,m)}$ describe the polariton damping rate and distance between the nanohole edge and AFM tip, respectively. In the calculations, $\tilde{\psi}_{PhPs,0}$, $R_{(n,m)}$, and $\gamma$ are set as 1, 1, and 0.15, $m$ and $n$ are set as 10 and 200. Note that the in-plane $q$ is strongly dependent on the propagation direction and can be rotation-controlled from Eq. S9. As shown in Fig. S8, the calculated field distributions using our phenomenological interference model show an excellent agreement with the measured near-field results.
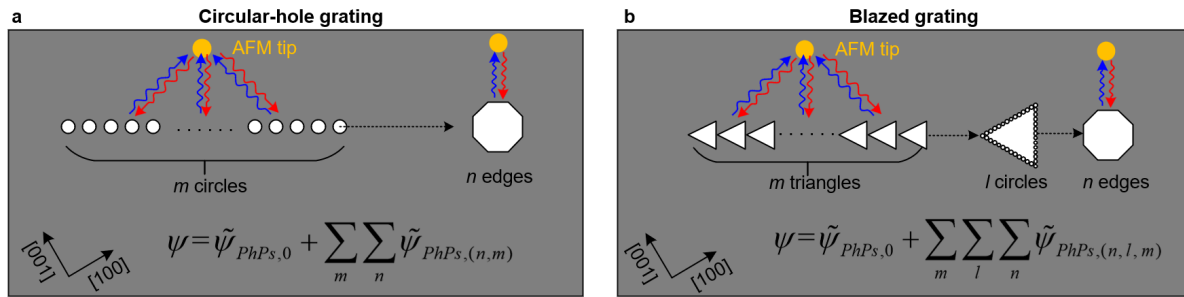


**Fig. S7 | Phenomenological interference model.** Illustration of the phenomenological interference model for (a) circular-hole grating and (b) blazed grating.

As for blazed grating (Fig. S7b), if only use three edges to configure above phenomenological interference model (Eq. S11), some diffraction signals may lose at the triangle apex. We therefore create $l$ small nanoholes (similar as dipole arrays) to mimic the triangle aperture. Indeed, the reflected PhPs near-filed patterns by a subwavelength slit (or triangle edge in Fig. S7b) is approximately that of a series nano-hole arrays. When many such nano-holes are arranged in a column with a spacing that is smaller than the PhP's wavelength, the reflected PhPs are plane waves that propagate perpendicularly away toward either side of the nano-hole column. Finally, the phenomenological interference model for blazed grating can be described as:

$$\psi = \tilde{\psi}_{PhPs,0} + \sum_m \sum_l \sum_n \tilde{\psi}_{PhPs,(n,l,m)} \tag{S12}$$

In the calculated near-field images (Fig. S11), *m, l* and *n* are set as 18, 20 and 200.
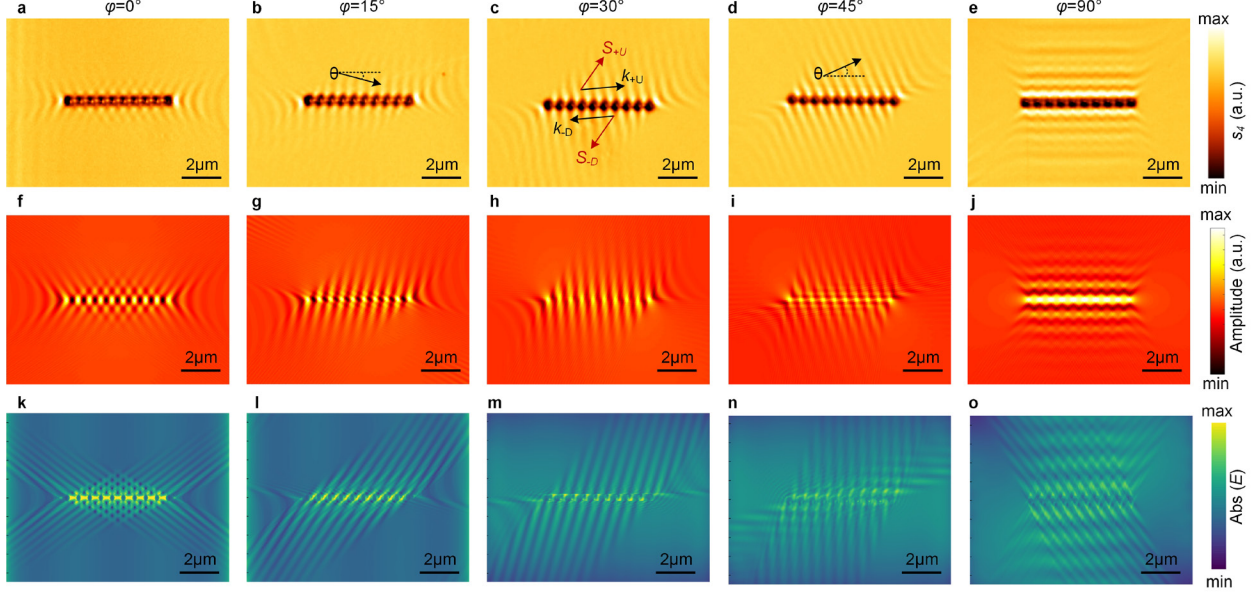


**Fig. S8 | Directional diffraction of PhPs at circular-hole gratings.** (a-e) Experimentally measured near-field amplitude images ($s_4$), (f-j) the calculated near-field pattern of diffracted tip-launched PhPs using phenomenological interference model, and (k-o) numerical simulated wavefront at different orientation angles. The frequency $\omega$=904 cm$^{-1}$, and 220 nm-thick $\alpha$-MoO$_3$ sample is placed on SiO$_2$/Si substrate, with grating period $\Lambda$=600 nm, and nano-hole diameter 300 nm.

## 8. Experimental observation of unidirectional grating-excited PhPs

According to polariton diffraction conditions: the grating's reciprocal lattice vector ($k_G = \pm 2\pi/\Lambda$) should have an intersection with the hyperbolic isofrequency contour, we can distinguish two case studies as shown in Fig. S9c and Fig. S9d.

**Case 1-Diffraction of tip-launched PhPs ($2k_{100}<k_G$):** as shown in Fig. S9c, because $\underline{k_G}$ has intersections with both the red and blue isofrequency contours, the diffraction condition is satisfied for both tip and grating launched PhPs. But the initial signal of tip-launched PhPs are stronger, as a result, the diffraction of tip-launched PhPs also creates stronger fringes through additive interference. Therefore, the near-field distributions are mostly attributed to the tip-launched PhPs. This case study was illustrated in Fig. 3 of the manuscript.

**Case 2-Diffraction of grating-excited PhPs ($k_{100}<k_G<2k_{100}$):** as shown in Fig. S9d, with a specific grating spacing, e.g., $\lambda_p/2<\Lambda<\lambda_p$, the diffraction of tip-launched PhPs is forbidden because $k_G<2k_{100}$, there has no intersection between $\underline{k_G}$ and the blue dashed isofrequency contour. While $k_G>k_{100}$ allows for diffraction of grating-excited PhPs. As a result, the sum of the grating-excited PhPs from each nanohole creates strong fringe intensity through additive interference. Thus, the

near-field distributions are mostly attributed to the grating-excited PhPs. This case study was illustrated in Fig. 4 of the manuscript.
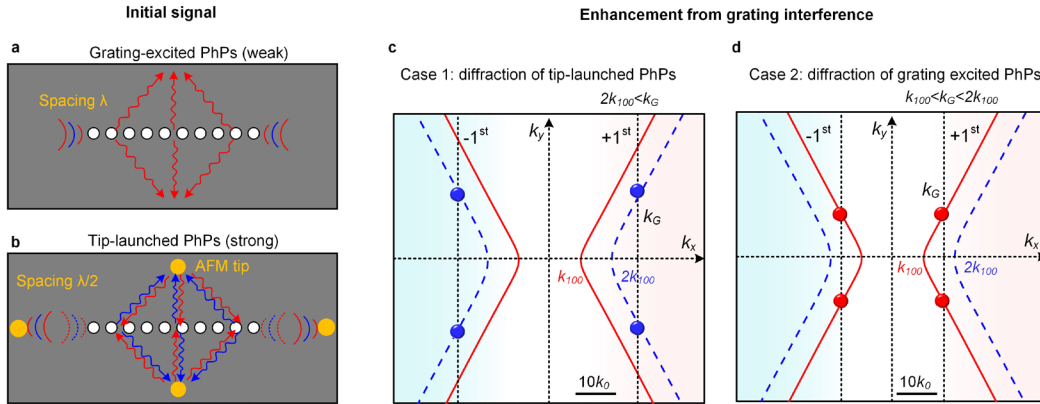


**Fig. S9 | The selection rules for grating diffraction of tip or grating launched PhPs.** (a, b) Schematics of (a) grating-excited PhPs and (b) tip-launched PhPs. (c, d) Case studies of diffraction of (c) tip-launched PhPs and (d) grating-excited PhPs according to momentum matching condition. With $2k_{100}<k_G$, the 1$^{st}$ order diffraction of tip-launched PhPs plays a major role (blue circles). With $k_{100}<k_G<2k_{100}$, the 1$^{st}$-order diffraction of tip-launched PhPs is forbidden, whereas the diffraction of grating-excited PhPs is possible because $k_G$ has intersections (red circles) with the red isofrequency contour.

Beyond 1$^{st}$ order diffraction, the gratings also generate high order modes. As shown in Fig. S10a, even though the 1$^{st}$ order diffraction of tip-launched PhPs is forbidden, the diffraction channel for 2$^{nd}$ order diffraction of tip-launched PhPs (green diamonds in Fig. S10a) is open because $2k_G>2k_{100}$, as demonstrated by phenomenological interference model calculated near-field image in Fig. S10c.
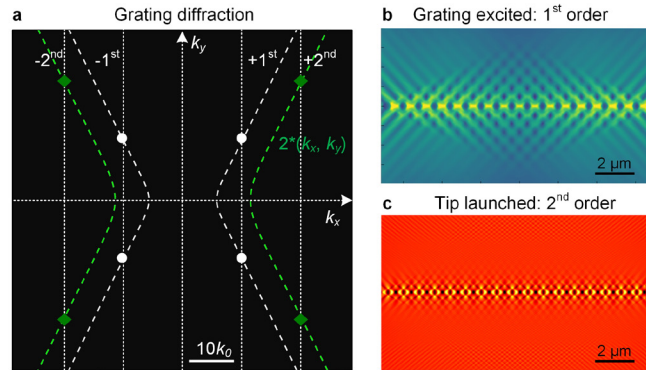


**Fig. S10 | The momentum matching in grating diffraction.** (a) With $k_{100}<k_G<2k_{100}$, the 1$^{st}$ order diffraction is from grating-excited PhPs (white circles), while tip-launched PhPs (green diamonds) plays a role only in the 2$^{nd}$ order diffraction. (b) The simulated wavefront shows the 1$^{st}$ order diffraction of grating excited PhPs, and (c) the calculated near-field image via phenomenological interference model shows the 2$^{nd}$ order diffraction of tip-launched PhPs.

Fig. S11(a-c) show the original data of s-SNOM near-field distributions by different nanogratings. It's clear that the original results contain all kinds of PhP modes (*e.g.*, 1$^{st}$ order, 2$^{nd}$ order, tip-launched and grating-excited PhPs). By performing FTs of the up-side and down-side near-field distributions in Fig. S11(a-c), we confirm that the highest FT spots (within white circles) in Figs. S11(d-f) belong to the 1$^{st}$ order diffraction of grating-excited PhPs, because they are located at the intersection of $k_P$ (white dashed line) and $k_G$ (grating reciprocal vector). Another two FT spots in

green circles belong to the 2$^{nd}$ order diffraction of tip-launched PhPs. To directly reveal the grating-excited PhPs, we applied removing masks [dashed rectangles in Fig. S11(d-f)] on the 2$^{nd}$ order tip-launched PhPs in the FT image. Then, the near-field images of 1$^{st}$ order diffraction of grating-excited PhPs have been restored by performing reverse FT, as shown in Fig. S11(g-i). In addition, to directly demonstrate the unidirectional contrast between two-side PhPs, we further performed FT of the up-side (red dashed box) and down-side (blue dashed box) parts in Fig. S11(g-i), where the middle grating parts have been removed in FT process, and then we obtain an intuitive comparison of the excitation efficiencies of two-side PhPs. Furthermore, the right-half image in dashed box in Fig. S11(J-L) correspond to FT of +1$^{st}$ order diffraction of PhPs, and the left-half image correspond to the FT of -1$^{st}$ order diffraction of PhPs. Then, we spliced the two half images in red and blue dashed boxes together into the final FT result as illustrated in Fig. 4(L to N) of the main-text.
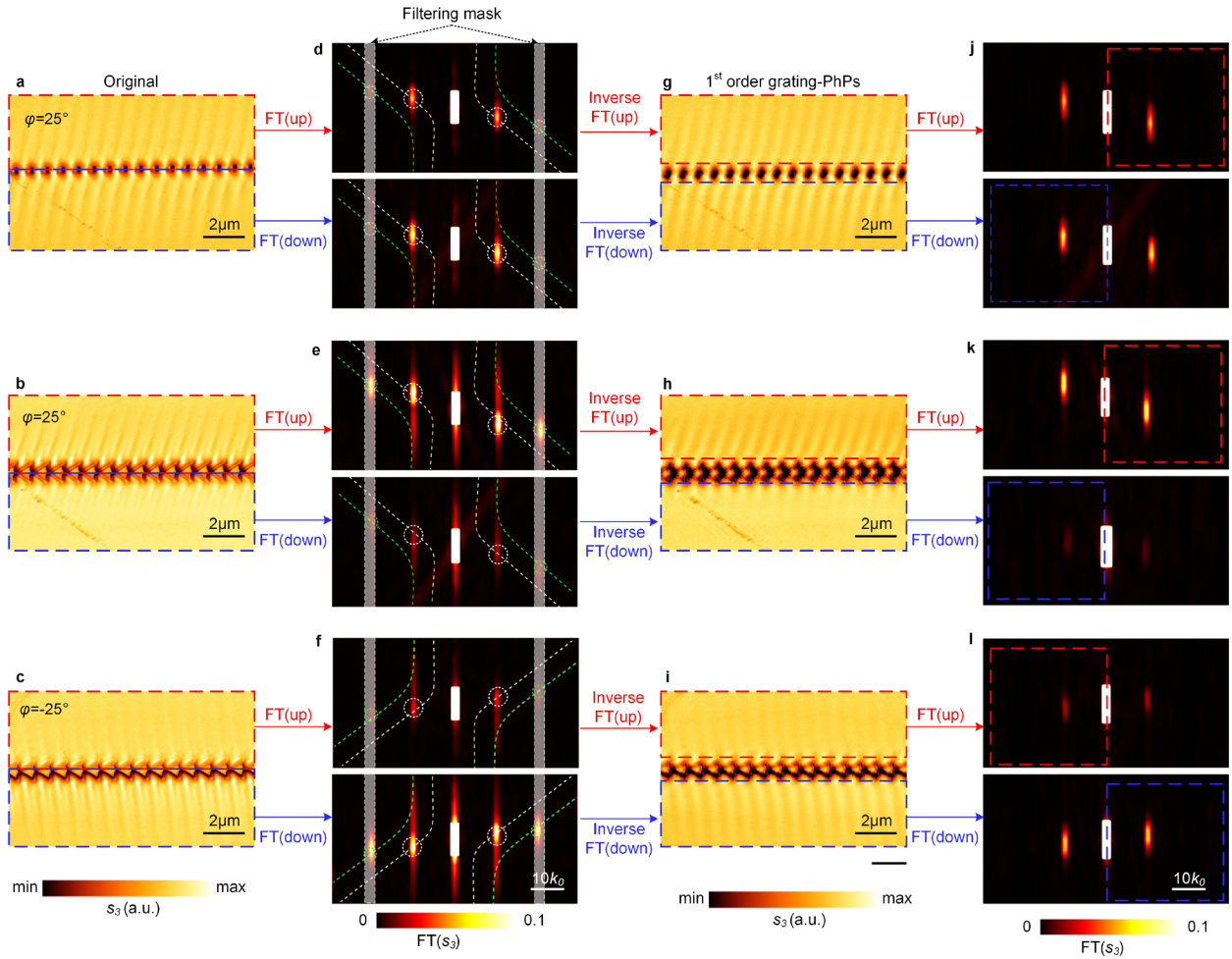


**Fig. S11 | Experimental results of grating-excited PhPs and their unidirectional diffraction.** (a-c) Experimentally measured near-field images of diffracted PhPs with (a) one circular-nanohole grating and (b, c) two blazed gratings with orientation angle $\varphi$=-25° and 25° at frequency 904 cm$^{-1}$. The α-MoO$_3$ sample thickness $d$=182nm, the grating period $\Lambda$=800 nm, circular-hole diameter 400 nm, and triangle size 800×1000 nm. (d-f) The FTs of the up-side and down-side near-field distributions in (a-c), in which the FT spots correspond to the diffraction states. The gray dashed rectangles in (d-f) represent the removing mask to filter out 2$^{nd}$ order tip-launched PhPs. (g-i) The filtered near-field images of the 1$^{st}$ order grating-excited PhPs restored by performing reverse FT of the results in (d-f). The circular-

hole grating generates both the forward and backward grating-excited PhPs, which belong to the +1st and -1st diffraction orders, respectively. The blazed grating enables unidirectional excitation of up-side or down-side grating-PhPs by inversing the orientation angle from -25° to +25°. (j-l) The FTs of the up-side (red dashed box) and down-side (blue dashed box) near-field distributions of the 1st order grating-excited PhPs in (g-i), respectively. The middle grating parts have been removed in FT process.
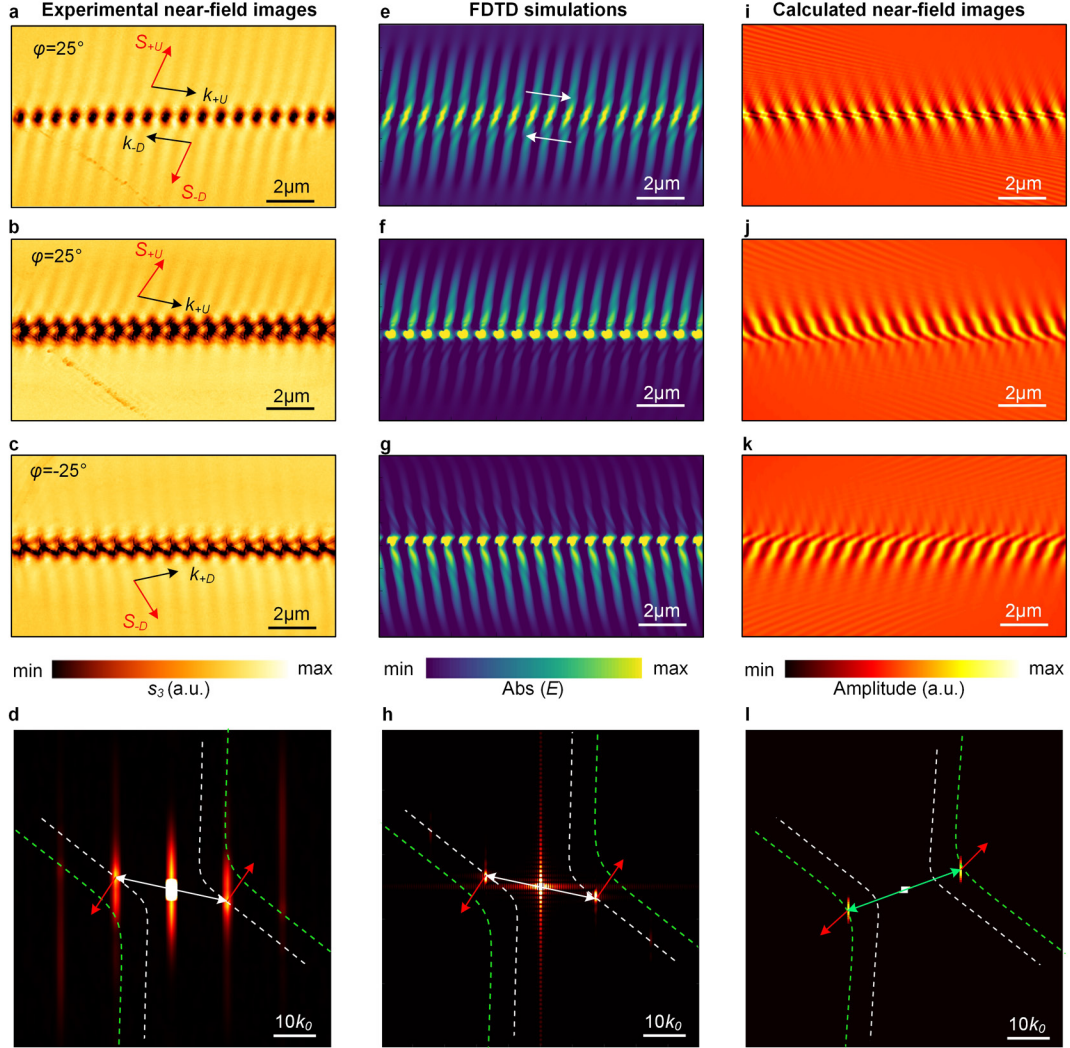


**Fig. S12 | The comparison between experiments, FDTD simulations and calculated near-field images.** (a-c) Experimentally measured near-field images at frequency 904 cm$^{-1}$. (d) The FT of the near-field distributions in (a), in which the bright FT intensity spots correspond to the 1st order diffraction of grating-excited PhPs. (e-g) The FDTD simulated electric field distributions (abs($E$)) and (h) the corresponding dispersion [FT of result in (e)] of grating-excited PhPs. (i-k) The phenomenological interference model calculated near-field images and (l) the corresponding dispersion [FT of result in (i)], showing the 1st order diffraction of tip-launched PhPs. Noting that the experimental results match well with the simulated results, further confirming that the strongest experimental fringes originate from the grating-excited PhPs. However, the calculated near-field images (i-k) and corresponding FT dispersion (l) mainly show the 1st diffraction of tip-launched PhPs, which are different from the filtered 1st order experimental results and simulations in (a-h).

The two-side intensities of grating-excited PhPs are affected by the grating orientation angle $\varphi$. To demonstrate this, we performed FDTD simulations to calculate the intensities of two-side PhPs (U,

D) as a function of rotation angle, as shown by the solid curves in Fig. S13i. In the FDTD simulation, two surface (along *xz* plane) power monitors [indicated by red and blue dashed lines in Fig. S13(a, b)] are set at two sides of the grating to collect the electric fields of excited PhPs, and the distance between power monitor and grating is set as 1000 nm. By integrating the electric fields recorded by these two power monitors, we obtained the output intensities of two-side PHPs, as shown in Fig. S13g, when $\varphi$ changes from 0° to 90°, the intensity of two states can be tuned with different values due to the asymmetric excitation. As for $\varphi$=25°, the intensity of +U state increases significantly while the intensity of -D state decreases to zero. Such a maximum intensity contrast between two states further manifests the unidirectional excitation of PhPs. To quantify the unidirectional contrast between experimentally measured two-side PhPs, we extracted FT spectra [Fig. S13(g, h)] along horizontal line cuts in Fig. S13(e, f) corresponding to up-side (red dashed lines) and down-side (blue dashed lines) excitations, respectively. By integrating the spectral weight, we found that the normalized excitation efficiencies for up/down PhPs are approximately 1/0.11 at $\varphi$=+25°, and 0.26/1 at $\varphi$=-25°. The normalized intencities are marked by symbols in Fig. S13i, which shows evident contrast of unidirectionality at $\varphi$=±25°.
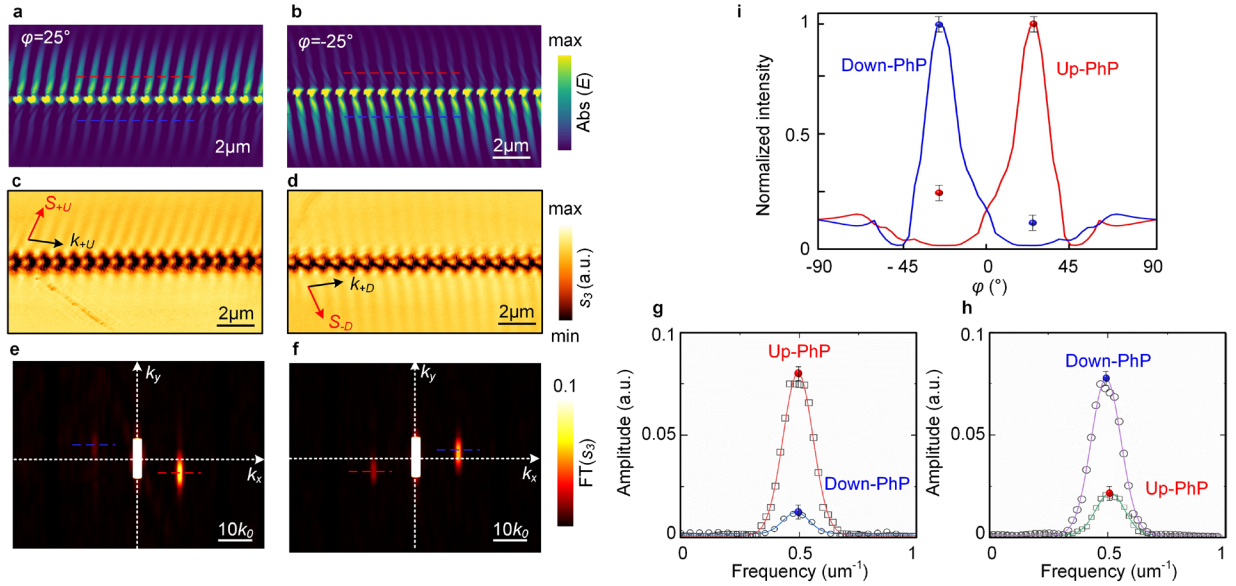


**Fig. S13 | The excitation differences between two-side PhPs.** (a, b) The simulated wavefronts and (c, d) experimentally measured near-field amplitude images of grating-excited PhPs at orientation angle $\varphi$=+25° and -25°, respectively. (e, f) The right and left spots off the center correspond to the FT intensity of forward (+1st order) and backward (-1st order) diffraction of grating-excited PhPs in (c, d). (g, h) The FT spectra along horizontal line cuts in (e, f) correspond to the FT intensities of PhPs propagating up-side and down-side the grating, respectively. (i) The solid curves are FDTD simulated intensities of two-side PhPs as a function of orientation angle $\varphi$. The symbols indicate the measured intensities of two-side PhPs by integrating the FT spectra in (g, h), which are 1/0.11 (up/down) and 0.26/1 (up/down) at $\varphi$=±25°, respectively.

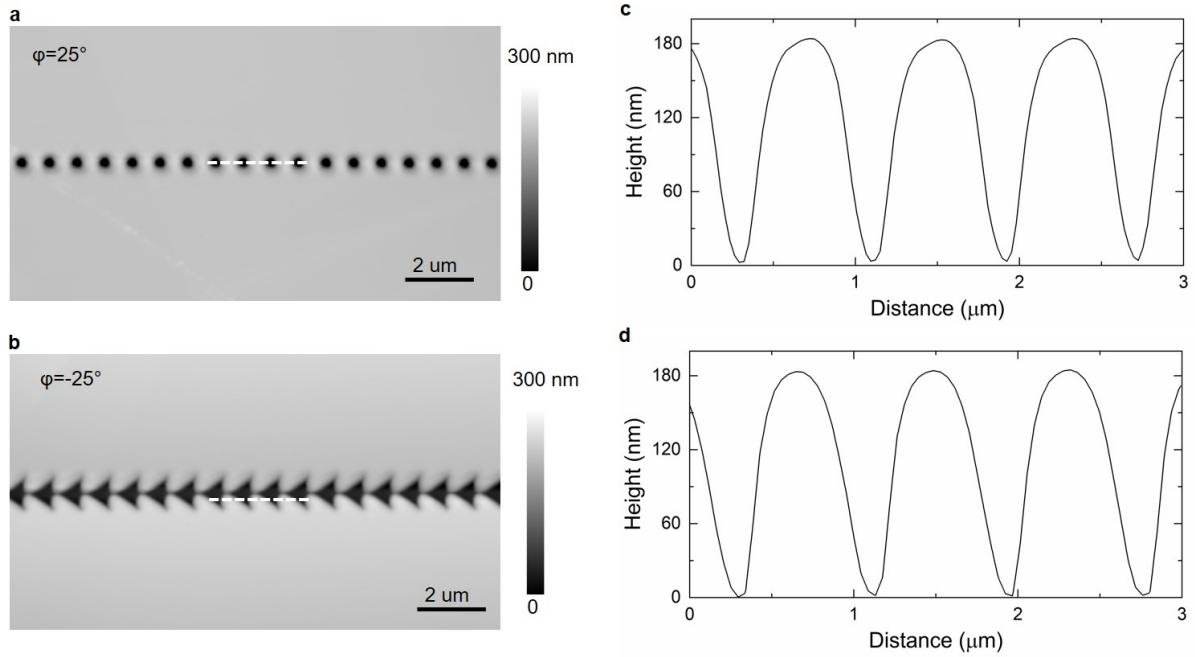**Fig. S14 | AFM results of patterned nano-gratings on α-MoO₃.** (a, b) AFM images and (c, d) line cuts of a 182 nm-thick α-MoO₃ sample with circular-hole and blazed gratings. The grating period $\Lambda$=800 nm, circular grating orientation angle $\varphi$=25°, circular-hole diameter 400 nm; and the triangle grating orientation angle $\varphi$=-25°, triangle size 800×1000 nm.

# REFERENCES AND NOTES

1. T. Low, A. Chaves, J. D. Caldwell, A. Kumar, N. X. Fang, P. Avouris, T. F. Heinz, F. Guinea, L. Martin-Moreno, F. Koppens, Polaritons in layered two-dimensional materials. *Nat. Mater.* **16**,182–194 (2017).

2. D. N. Basov, M. M. Fogler, F. J. G. de Abajo, Polaritons in van der Waals materials. *Science* **354**, aag1992 (2016).

3. R. Hillenbrand, T. Taubner, F. Keilmann, Phonon-enhanced light–matter interaction at the nanometre scale. *Nature* **418**, 159–162 (2002).

4. S. Dai, Z. Fei, Q. Ma, A. S. Rodin, M. Wagner, A. S. McLeod, M. K. Liu, W. Gannett, W. Regan, K. Watanabe, T. Taniguchi, M. Thiemens, G. Dominguez, A. H. C. Neto, A. Zettl, F. Keilmann, P. Jarillo-Herrero, M. M. Fogler, D. N. Basov, Tunable phonon polaritons in atomically thin van der Waals crystals of boron nitride. *Science* **343**, 1125–1129 (2014).

5. P. Li, X. Yang, T. W. W. Maß, J. Hanss, M. Lewin, A.K. U. Michel, M. Wuttig, T. Taubner, Reversible optical switching of highly confined phonon–polaritons with an ultrathin phase-change material. *Nat. Mater.* **15**, 870–875 (2016).

6. W. Ma, G. Hu, D. Hu, R. Chen, T. Sun, X. Zhang, Q. Dai, Y. Zeng, A. Alù, C.W. Qiu, P. Li, Ghost hyperbolic surface polaritons in bulk anisotropic crystals. *Nature* **596**, 362–366 (2021).

7. F. H. Feres, R. A. Mayer, L. Wehmeier, F. C. B. Maia, E. R. Viana, A. Malachias, H. A. Bechtel, J. M. Klopf, L. M. Eng, S. C. Kehr, J. C. González, R. O. Freitas, I. D. Barcelos, Sub-diffractional cavity modes of terahertz hyperbolic phonon polaritons in tin oxide. *Nat. Commun.* **12**, 1–9 (2021).

8. W. Ma, P. Alonso-González, S. Li, A. Y. Nikitin, J. Yuan, J. Martín-Sánchez, J. Taboada-Gutiérrez, I. Amenabar, P. Li, S. Vélez, C. Tollan, Z. Dai, Y. Zhang, S. Sriram, K. Kalantar-Zadeh, S.T. Lee, R. Hillenbrand, Q. Bao, In-plane anisotropic and ultra-low-loss polaritons in a natural van der Waals crystal. *Nature* **562**, 557–562 (2018).

9. J. Taboada-Gutiérrez, G. Álvarez-Pérez, J. Duan, W. Ma, K. Crowley, I. Prieto, A. Bylinkin, M. Autore, H. Volkova, K. Kimura, T. Kimura, M.H. Berger, S. Li, Q. Bao, X. P. A. Gao, I. Errea, A. Y. Nikitin, R. Hillenbrand, J. Martín-Sánchez, P. Alonso-González, Broad spectral tuning of ultra-low-loss polaritons in a van der Waals crystal by intercalation. *Nat. Mater.* **19***,* 964–968 (2020).

10. N. C. Passler, X. Ni, G. Hu, J. R. Matson, G. Carini, M. Wolf, M. Schubert, A. Alù, J. D. Caldwell, T. G. Folland, A. Paarmann, Hyperbolic shear polaritons in low-symmetry crystals. *Nature* **602,** 595–600 (2022).

11. G. Hu, Q. Ou, G. Si, Y. Wu, J. Wu, Z. Dai, A. Krasnok, Y. Mazor, Q. Zhang, Q. Bao, C.W. Qiu, A. Alù, Topological polaritons and photonic magic angles in twisted α-MoO$_3$ bilayers. *Nature* **582**, 209–213 (2020).

12. S.-H. Gong, F. Alpeggiani, B. Sciacca, E. C. Garnett, L. Kuipers, Nanoscale chiral valley-photon interface through optical spin-orbit coupling. *Science* **359**, 443–447 (2018).

13. L. Sun, C.Y. Wang, A. Krasnok, J. Choi, J. Shi, J. S. Gomez-Diaz, A. Zepeda, S. Gwo, C.K. Shih, A. Alù, X. Li, Separation of valley excitons in a MoS 2 monolayer using a subwavelength asymmetric groove array. *Nat. Photonics* **13**, 180–184 (2019).

14. S. Guddala, F. Komissarenko, S. Kiriushechkina, A. Vakulenko, M. Li, V. M. Menon, A. Alù, A. B. Khanikaev, Topological phonon-polariton funneling in midinfrared metasurfaces. *Science* **374**, 225–227 (2021).

15. W. Liu, Z. Ji, Y. Wang, G. Modi, M. Hwang, B. Zheng, V. J. Sorger, A. Pan, R. Agarwal, Generation of helical topological exciton-polaritons. *Science* **370**, 600–604 (2020).

16. J. Duan, G. Álvarez-Pérez, A. I. F. Tresguerres-Mata, J. Taboada-Gutiérrez, K. V. Voronin, A. Bylinkin, B. Chang, S. Xiao, S. Liu, J. H. Edgar, J. I. Martín, V. S. Volkov, R. Hillenbrand, J. Martín-Sánchez, A. Y. Nikitin, P. Alonso-González, Planar refraction and lensing of highly confined polaritons in anisotropic media. *Nat. Commun.* **12**, 4325 (2021).

17. T. G. Folland, A. Fali, S. T. White, J. R. Matson, S. Liu, N. A. Aghamiri, J. H. Edgar, R. F. Haglund Jr, Y. Abate, J. D. Caldwell, Reconfigurable infrared hyperbolic metasurfaces using phase change materials. *Nat. Commun.* **9**, 1–7 (2018).

18. K. Chaudhary, M. Tamagnone, X. Yin, C. M. Spägele, S. L. Oscurato, J. Li, C. Persch, R. Li, N. A. Rubin, L. A. Jauregui, K. Watanabe, T. Taniguchi, P. Kim, M. Wuttig, J. H. Edgar, A. Ambrosio, F. Capasso, Polariton nanophotonics using phase-change materials. *Nat. Commun.* **10**, 1–6 (2019).

19. J. Duan, G Álvarez-Pérez, K. V. Voronin, I. Prieto, J. Taboada-Gutiérrez, V. S. Volkov, J. Martín-Sánchez, A. Y. Nikitin, P. Alonso-González, Enabling propagation of anisotropic polaritons along forbidden directions via a topological transition. *Sci. Adv.* **7**, eabf2690 (2021).

20. Q. Zhang, Q. Ou, G. Hu, J. Liu, Z. Dai, M. S. Fuhrer, Q. Bao, C.W. Qiu, Hybridized hyperbolic surface phonon polaritons at α-MoO$_3$ and polar dielectric interfaces. *Nano Lett.* **21**, 3112–3119 (2021).

21. F. J. Rodríguez-Fortuño, G. Marino, P. Ginzburg, D. O'Connor, A. Martínez, G. A. Wurtz, A. V. Zayats, Near-field interference for the unidirectional excitation of electromagnetic guided modes. *Science* **340**, 328–330 (2013).

22. J. Lin, J. P. B. Mueller, Q. Wang, G. Yuan, N. Antoniou, X.C. Yuan, F. Capasso, Polarization-controlled tunable directional coupling of surface plasmon polaritons. *Science* **340**, 331–334 (2013).

23. Z. Zheng, N. Xu, S. L. Oscurato, M. Tamagnone, F. Sun, Y. Jiang, Y. Ke, J. Chen, W. Huang, W. L. Wilson, A. Ambrosio, S. Deng, H. Chen, A mid-infrared biaxial hyperbolic van der Waals crystal. *Sci. Adv.* **5**, eaav8690 (2019).

24. G. Á.-Pérez, T. G. Folland, I. Errea, J. T.a-Gutiérrez, J. Duan, J. M.-Sánchez, A. I. F. T.-Mata, J. R. Matson, A. Bylinkin, M. He, W. Ma, Q. Bao, J. I. Martín, J. D. Caldwell, A. Y. Nikitin, P. Alonso-González, Infrared permittivity of the biaxial van der Waals semiconductor α-MoO$_3$ from near-and far-field correlative studies. *Adv. Mater.* **32**, 1908176 (2020).

25. J. Chen, M. Badioli, P. Alonso-González, S. Thongrattanasiri, F. Huth, J. Osmond, M. Spasenović, A. Centeno, A. Pesquera, P. Godignon, A. Zurutuza Elorza, N. Camara, F. J. G. de Abajo, R. Hillenbrand, F. H. L. Koppens, Optical nano-imaging of gate-tunable graphene plasmons. *Nature* **487**, 77–81 (2012).

26. Z. Fei, A. S. Rodin, G. O. Andreev, W. Bao, A. S. McLeod, M. Wagner, L. M. Zhang, Z. Zhao, M. Thiemens, G. Dominguez, M. M. Fogler, A. H. C. Neto, C. N. Lau, F. Keilmann, D. N. Basov, Gate-tuning of graphene plasmons revealed by infrared nano-imaging. *Nature* **487**, 82–85 (2012).

27. J. A. Gerber, S. Berweger, B. T. O'Callahan, M. B. Raschke, Phase-resolved surface plasmon interferometry of graphene. *Phys. Rev. Lett.* **113**, 055502 (2014).

28. W. Huang, F. Sun, Z. Zheng, T. G. Folland, X. Chen, H. Liao, N. Xu, J. D. Caldwell, H. Chen, S. Deng, Van der Waals phonon polariton microstructures for configurable infrared electromagnetic field localizations. *Adv. Sci.* **8**, 2004872 (2021).

29. A. J. Sternbach, S. H. Chae, S. Latini, A. A. Rikhter, Y. Shao, B. Li, D. Rhodes, B. Kim, P. J. Schuck, X. Xu, X.-Y. Zhu, R. D. Averitt, J. Hone, M. M. Fogler, A. Rubio, D. N. Basov, Programmable hyperbolic polaritons in van der Waals semiconductors. *Science* **371**, 617–620 (2021).

30. C. Wang, S. Huang, Q. Xing, Y. Xie, H. Yan, Van der Waals thin films of $WTe_2$ for natural hyperbolic plasmonic surfaces. *Nat. Commun.* **11**, 1158 (2020).

31. F. Wang, C. Wang, A. Chaves, C. Song, G. Zhang, S. Huang, Y. Lei, Q. Xing, L. Mu, Y. Xie, H. Yan, Prediction of hyperbolic exciton-polaritons in monolayer black phosphorus. *Nat. Commun.* **12**, 1–7 (2021).

32. A. Huber, N. Ocelic, R. Hillenbrand, Local excitation and interference of surface phonon polaritons studied by near-field infrared microscopy. *J. Microsc.* **229**, 389–395 (2008).

33. Q. Zhang, G. Hu, W. Ma, P. Li, A. Krasnok, R. Hillenbrand, A. Alù, C.W. Qiu, Interface nano-optics with van der Waals polaritons. *Nature* **597**, 187–195 (2021).

34. L. Xiong, C. Forsythe, M. Jung, A. S. McLeod, S. S. Sunku, Y. M. Shao, G. X. Ni, A. J. Sternbach, S. Liu, J. H. Edgar, E. J. Mele, M. M. Fogler, G. Shvets, C. R. Dean, D. N. Basov, Photonic crystal for graphene plasmons. *Nat. Commun.* **10**, 4780 (2019).

35.  L. Xiong, Y. Li, M. Jung, C. Forsythe, S. Zhang, A. S. McLeod, Y. Dong, S. Liu, F. L. Ruta, C. Li, K. Watanabe, T. Taniguchi, M. M. Fogler, J. H. Edgar, G. Shvets, C. R. Dean, D. N. Basov, Programmable Bloch polaritons in graphene. *Sci. Adv.* **7**, eabe8087 (2021).

36.  Z. Dai, G. Hu, G. Si, Q. Ou, Q. Zhang, S. Balendhran, F. Rahman, B. Y. Zhang, J. Z. Ou, G. Li, A. Alù, C.W. Qiu, Q. Bao, Edge-oriented and steerable hyperbolic polaritons in anisotropic van der Waals nanocavities. *Nat. Commun.* **11**, 6086 (2020).

37.  A. Vakil, N. Engheta, Transformation optics using graphene. *Science* **332**, 1291–1294 (2011).

38.  A. Woessner, Y. Gao, I. Torre, M. B. Lundeberg, C. Tan, K. Watanabe, T. Taniguchi, R. Hillenbrand, J. Hone, M. Polini, F. H. L. Koppens, Electrical $2\pi$ phase control of infrared light in a 350-nm footprint using graphene plasmons. *Nat. Photonics* **11**, 421–424 (2017).

39.  Y. Wu, Q. Ou, Y. Yin, Y. Li, W. Ma, W. Yu, G. Liu, X. Cui, X. Bao, J. Duan, G. Álvarez-Pérez, Z. Dai, B. Shabbir, N. Medhekar, X. Li, C.M. Li, P. Alonso-González, Q. Bao, Chemical switching of low-loss phonon polaritons in $\alpha$-$MoO_3$ by hydrogen intercalation. *Nat. Commun.* **11**, 1–8 (2020).

40.  J. D. Caldwell, L. Lindsay, V. Giannini, I. Vurgaftman, T. L. Reinecke, S. A. Maier, O. J. Glembocki, Low-loss, infrared and terahertz nanophotonics using surface phonon polaritons. *Nanophotonics* **4**, 44–68 (2015).

41.  G. Álvarez-Pérez, K. V. Voronin, V. S. Volkov, P. Alonso-González, A. Y. Nikitin, Analytical approximations for the dispersion of electromagnetic modes in slabs of biaxial crystals. *Phys. Rev. B* **100**, 235408 (2019).

42.  Sun, F., Huang W., Zheng Z., Xu N., Ke Y., Zhan R., Chen H., Deng S. Polariton waveguide modes in two-dimensional van der Waals crystals: An analytical model and correlative nano-imaging. *Nanoscale* **13**, 4845–4854 (2021).